The Dwarf Irregular Galaxy Sextans A. I. HST Photometry of the Resolved Stars

Dohm-Palmer, Robbie C.; Skillman, Evan D.; Saha, A.; Tolstoy, E.; Mateo, Mario; Gallagher, J.; Hoessel, J.; Chiosi, C.; Dufour, R.~J.

Published in:
The Astronomical Journal

DOI:
10.1086/118664

Publication date:
1997

THE ASTRONOMICAL JOURNAL VOLUME 114, NUMBER 6 DECEMBER 1997

THE DWARF IRREGULAR GALAXY SEXTANS A. I. *HST* PHOTOMETRY OF THE RESOLVED STARS[1]

ROBBIE C. DOHM-PALMER AND EVAN D. SKILLMAN

Department of Astronomy, University of Minnesota, Minneapolis, Minnesota 55455
Electronic mail: robbie@astro.spa.umn.edu, skillman@astro.spa.umn.edu

A. SAHA

STScI, 3700 San Martin Drive, Baltimore, Maryland 21218
Electronic mail: saha@stsci.edu

E. TOLSTOY

ESO-ECF, Karl-Schwarzschild-Str. 2, D-85748 Garching b. München, Germany
Electronic mail: etolstoy@eso.org

MARIO MATEO

Department of Astronomy, University of Michigan, 821 Dennison Building, Ann Arbor, Michigan 48109-1090
Electronic mail: mateo@astro.lsa.umich.edu

J. GALLAGHER AND J. HOESSEL

Department of Astronomy, University of Wisconsin, 475 N. Charter Street, Madison, Wisconsin 53706-1582
Electronic mail: jsg@jayg.astro.wisc.edu, hoessel@jth.astro.wisc.edu

C. CHIOSI

Dipartimento Di Astronomia, 35122, Padova, PD, Italy
Electronic mail: chiosi@astrpd.pd.astro.it

R. J. DUFOUR

Department of Space Physics and Astronomy, Rice University, Box 1892, SS Building, Room 232, Houston, Texas 77251-1982
Electronic mail: rjd@regulus.rice.edu

Received 1997 June 19; revised 1997 August 19; accepted 1997 August 20

ABSTRACT

We have used the *Hubble Space Telescope* to observe the resolved stars of the nearby ($D=1.4$ Mpc) dwarf irregular galaxy Sextans A (DDO 75, A 1008-04). The data consist of dithered WFPC2 images in 3 bands: F439W (1 hour), F555W (30 minutes), and F814W (30 minutes). The stellar photometry was extracted using the DoPHOT program developed by Schechter *et al.* (1993, PASP, 105, 1342) with modifications for WFPC2 data by Saha *et al.* (1996, ApJ, 466, 550). The dithering improved the photometric accuracy of faint stars since it produced stellar profiles that were more uniform than in undithered images. Also, the PSF fitting method used by DoPHOT was insensitive to the intra-pixel sensitivity variation of the WFPC2 chips, while simple aperture photometry was slightly sensitive to this variation. The photometry was calibrated to V, B, and I with the equations presented in Holtzman *et al.* (1995, PASP, 107, 1065). Comparisons with previously published ground-based data showed excellent agreement with stars brighter than $V\approx 21$. Fainter stars are severely hampered by crowding from the ground. At the distance of Sextans A, the superior resolution of the *HST* overcomes this confusion, and enables very accurate and deep photometry. Artificial star tests showed the data to be 50% complete to $V=25.6$, $B=25.4$, and $I=25.3$. This high quality data produced color-magnitude diagrams (CMDs) with excellent detail. The main sequence (MS), red supergiants, and red giant branch (RGB) are all clearly distinct populations. Most striking is a population just redward of the MS, which had not been photometrically resolved from the MS in ground-based observations. These stars are massive core Helium burning stars (HeB) in the bluest extent of the so-called "blue-loop" phase. This population has never before been clearly identifiable in a low metallicity system.
 [S0004-6256(97)00612-2]

[1]Based on observations with the NASA/ESA *Hubble Space Telescope* obtained at the Space Telescope Science Institute, which is operated by the Association of Universities for Research in Astronomy, under NASA contract NAS 5-26555.

 0004-6256/97/114(6)/2514/13/$10.00

1. INTRODUCTION

Dwarf irregular (dI) galaxies are excellent laboratories for studying the star formation process. They are gas-rich, show little differential rotation, and contain active star formation (see Gallagher & Hunter 1984). In addition, they have low metallicity, and a reduced abundance of dust (relative to our Galaxy), which are conditions thought to exist in the early universe. The simpler dynamics may make them easier to study than larger spiral galaxies (but, see Skillman 1996 for a counter argument). In addition, the stellar properties of these galaxies provide a test for the accuracy of modern stellar evolution models at very low metallicity. For these reasons, dI galaxies are powerful tools for revealing the physical processes of galaxy formation and evolution.

The star formation process is most directly probed by determining the star formation history (SFH) of the galaxy. For galaxies in or near the Local Group, it is possible to obtain photometry of the resolved stars and observe star formation events directly from the color-magnitude diagram (CMD). The Carina Dwarf Spheroidal is an excellent example (Smecker-Hane *et al.* 1994). The LMC and SMC are the closest gas-rich candidates, and recent work has extracted their SFHs from stellar populations (e.g., Mateo 1988; Bertelli *et al.* 1992; Gallagher *et al.* 1996). However, interaction with our Galaxy complicates their evolution.

Many excellent attempts have been made from the ground to obtain SFHs of noninteracting dI's. Several examples include Sextans B (Tosi *et al.* 1991), NGC 6822 (Marconi *et al.* 1995; see also Gallart *et al.* 1996a, 1996b, 1996c), and Leo A (Tolstoy 1996). Unfortunately, these methods have been limited by the depth and accuracy of photometry available from the ground. Vast improvement can be made through use of the *Hubble Space Telescope* (*HST*). The superior angular resolution of the *HST* defeats much of the crowding of stellar images which greatly affects stellar photometry in systems at distances of order 1 Mpc. This allows deeper and more accurate photometry than possible from the ground.

Sextans A (DDO 75, A 1008-04) is a gas-rich dI (Skillman *et al.* 1988) with active star formation. It has Galactic coordinates $l=246°$, $b=40°$ and Heliocentric systemic velocity 325 km s^{-1} (Skillman *et al.* 1988). It is low surface brightness with an apparent magnitude $m_B=11.86$, and a color index $B-V=0.26$ (Hunter & Plummer 1996). Its metallicity has been measured to be $\sim 4\%$ solar from H II region spectroscopy (Skillman *et al.* 1989). The H II regions have been catalogued by Hodge *et al.* (1994) and Aparicio & Rodriguez-Ulloa (1992). The H I is concentrated in two clumps, which correspond to the major star forming regions (Skillman *et al.* 1988). The H I observations also indicate that the gas rotates in solid body rotation, but the axis of rotation is not aligned with the optical axis of symmetry, indicative of a barred galaxy. The optical component has a peculiar square shape, which may be related to such a kinematic bar.

Sextans A is located on the periphery of the Local Group. Sandage & Carlson (1982) derive a distance modulus of 25.67 ($D=1.3$ Mpc) from photographic photometry of Cepheid variable stars. Piotto *et al.* (1994) added five more Cepheids to those already known. They found a distance modulus of 25.71 (1.4 Mpc) ± 0.20, which has been revised to 25.33 (1.2 Mpc) by Richer & McCall (1995). Sakai *et al.* (1996, hereafter S96) derive an alternative distance modulus of 25.74 (1.41 Mpc) from the tip of the red-giant branch, and 25.85 (1.47 Mpc) from a re-analysis of all known Cepheid stars. We adopt a distance modulus of 25.8 (1.44 Mpc). Sextans A has a diameter $D_{25}=5'.9$ (de Vaucoulers *et al.* 1991), corresponding to 2.5 kpc at this distance.

TABLE 1. Cycle 5 *HST* observations of Sextans A.

Date	Instrument	Filter	Exposure (sec)
1 Dec. 1995	WFPC2	F439W	2×900, 2×1100
		F555W	3×600
		F814W	3×600

Previous ground-based studies of the stellar population have been conducted by several groups. Sandage & Carlson (1982) examined the brightest stars from photographic plates in B and V. Hoessel *et al.* (1983) obtained CCD photometry in the Gunn filter system, and made initial attempts at a star formation history. Walker (1987) obtained CCD photometry in B and V of the brightest stars, resulting in a revision of the distance modulus. Aparicio *et al.* (1987, hereafter A87) continued the SFH study with CMDs in UBV down to a limiting magnitude of 23.6 in V. Finally, S96 measured stars in V and I to a V limit of ~ 23. Despite excellent efforts, the CMDs of these ground-based studies are severely hampered by crowding problems.

This paper (Paper I) describes in detail the photometric measurement and calibration of the resolved stars in Sextans A. We first describe the observations and photometric measurement using DoPHOT. We discuss the effects of dithering and intra-pixel sensitivity with regards to the undersampled PSF of the WFPC2 images. We also examine the noise contributed by the matching of stars between filters. The next section discusses the calibration of the data to the Johnson B, V and Cousins I filter system, including corrections for interstellar reddening. We then determine the completeness levels for our data based on false star measurements. Finally, we present the CMDs and discuss them qualitatively. Paper II (Dohm-Palmer *et al.* 1997) will determine the recent SFH over the past 600 Myr directly from star counts in the CMD. Paper III will present an analysis using Bayesian Statistical Inference (Tolstoy & Saha 1996) to extend the SFH beyond 1 Gyr.

2. OBSERVATIONS AND PHOTOMETRIC EXTRACTION

2.1 DoPHOT and Error Analysis

The *HST* observations were obtained on 1995 December 1, and consisted of WFPC2 images in three filters: F439W (4000 s), F555W (1800 s) and F814W (1800 s). A summary of the *HST* observations is provided in Table 1. Figure 1 (Plate 113) is a true color image of the WFPC2 field, along

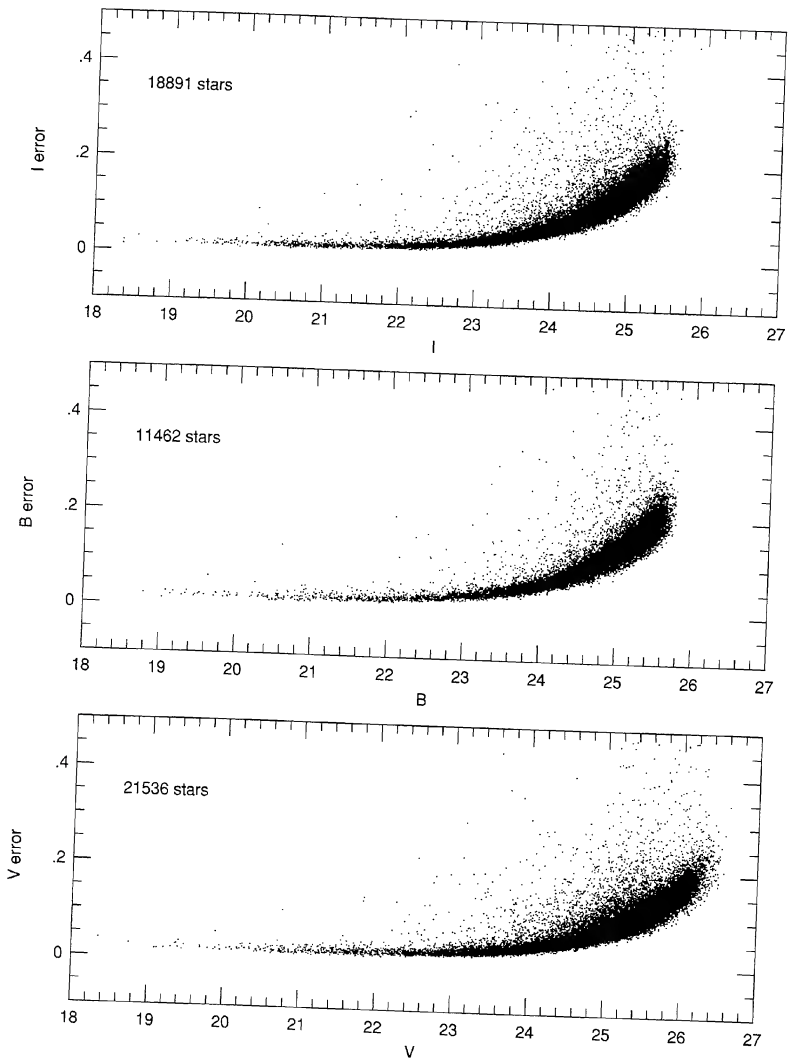

FIG. 2. The points show the distribution of internal errors with magnitude as determined by DoPHOT. The vast majority of the stars lie along a single curve that rises and increases in width toward fainter magnitudes. The highest error on this curve is ~0.25. The scatter of points above this curve comprise only ~1% of the data. The deepest photometry is in V, followed by B and then I.

with a Digitized Sky Survey image.[2] The images were calibrated with the standard STSDAS pipeline reduction. We employed a dithering technique for the exposures in order to simultaneously reject cosmic ray hits and "warm pixels" and to partially compensate for the undersampled point spread function (PSF) of the WF images (Burrows 1994). The dithering offsets between exposures within each filter were two pixels plus a fractional pixel amount. They were aligned to within the nearest whole pixel before the exposures were coadded. Cosmic rays were detected and corrected during the coadding of exposures with an anticoincidence technique between pairs of images. Because the WFPC2 PSF is undersampled, stars will often be flagged using the standard anti-coincidence techniques. Therefore, we used a technique described in Saha *et al.* (1996) which was developed to preserve true stars in the undersampled images.

The photometry was measured from the coadded images using the DoPHOT program (Schechter *et al.* 1993), which employs a model fitting technique rather than aperture photometry. We used a version of DoPHOT optimized for the undersampled WFPC2 PSF, as described in Saha *et al.* (1996). The internal measurement errors are shown in Fig. 2. We obtain the deepest photometry in V, followed by B and then I. The vast majority of points are clustered along a curve that both increases to ~0.25 and gets broader toward fainter magnitudes. The scatter of points above the main curve is only ~1% of the stars.

WFPC2 pixels are not uniformly sensitive within their boundaries. There are some parts of the pixel that do not

[2]The Digitized Sky Surveys were produced at the Space Telescope Science Institute under U.S. Government grant NAG W-2166. The images of these surveys are based on photographic data obtained using the Oschin Schmidt Telescope on Palomar Mountain and the UK Schmidt Telescope. The plates were processed into the present compressed digital form with the permission of these institutions.

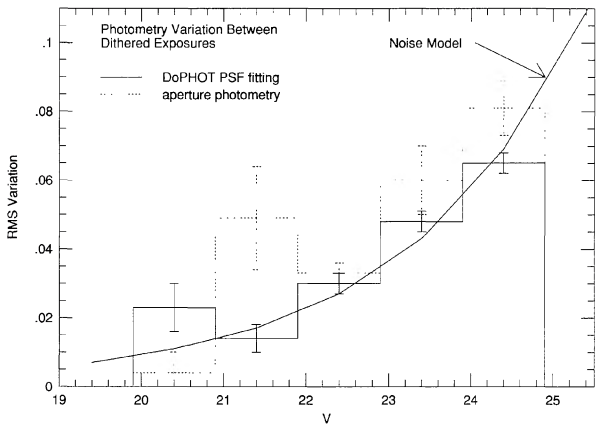

FIG. 3. The dithered exposures allowed us to see if the WFPC2 intra-pixel sensitivity variation affected the photometry. The solid histogram shows the rms variation of magnitude when measuring the same stars in the three separate exposures of chip 3 in F555W. The dotted histogram is the rms variation for the same stars when measured with a 0.″5 aperture. Only the brightest stars were measured. The curve is a simple noise model that includes read and Poisson counting noise. The PSF fitting histogram follows the noise model, indicating that the intra-pixel sensitivity variation does not contribute to the photometry error. By comparison, the aperture photometry histogram lies slightly above this curve, indicating an additional noise source.

detect incident flux (Burrows 1994). Aperture photometry is sensitive to this because ~65% of a point source's light falls within a single pixel. Therefore, the detected flux from a point source depends upon where the center falls within the pixel. We can take advantage of the dithering scheme to measure the effect of intra-pixel sensitivity variation. We used DoPHOT to measure the photometry of the brightest stars in the three F555W exposures of chip 3 prior to coadding and cosmic ray rejection. We also performed aperture photometry on the same star set. Figure 3 shows the rms variation of the photometry from both methods compared to a simple noise model that includes Poisson and read noise. The variation in DoPHOT photometry between the different exposures follows the noise model, while the aperture photometry variation is slightly higher. This indicates that the PSF fitting method is able to compensate for the intra-pixel sensitivity variation, to which simple aperture photometry is susceptible.

The dithering does prove beneficial for the accuracy of faint stars. After coadding the dithered images, the stellar profiles were much more symmetric and uniform across the chip. For example, the rms variation of the shape parameters, σ_x and σ_y [see Eq. (2)], for the stellar fits was 0.5 in the individual exposures compared to 0.2 in the coadded image. This uniformity greatly aids in accurately measuring the photometry as well as distinguishing between stellar objects and nonstellar objects.

In order for DoPHOT to identify stellar objects in the images, we needed to specify an approximate shape for the PSF. DoPHOT uses a modified Gaussian expansion for its model PSF:

$$I(x,y)=I_0[1+z^2+\tfrac{1}{2}\beta_4(z^2)^2+\tfrac{1}{6}\beta_6(z^2)^3+\tfrac{1}{24}\beta_8(z^2)^4]^{-1}+I_s, \quad (1)$$

TABLE 2. DoPHOT PSF shape parameters.

Filter	Chip	σ	β_4	β_6	β_8
B	1 (PC)	0.8	1.9	−0.1	0.0
	2	0.7	1.5	0.5	0.2
	3	0.7	2.2	−0.8	0.3
	4	0.7	2.1	−0.5	0.3
V	1 (PC)	0.8	3.9	−4.3	2.2
	2	0.7	2.4	−0.9	0.4
	3	0.7	2.1	−0.5	0.2
	4	0.7	2.4	−0.8	0.3
I	1 (PC)	0.8	3.7	−3.2	1.1
	2	0.7	2.9	−2.1	1.3
	3	0.7	2.4	−1.2	0.5
	4	0.7	2.0	−0.3	0.1

where

$$z^2=\frac{1}{2}\left(\frac{x^2}{\sigma_x^2}+2\sigma_{xy}xy+\frac{y^2}{\sigma_y^2}\right), \quad (2)$$

I_0 is the peak intensity, I_s is the sky intensity, and σ is the Gaussian standard deviation. The shape of this analytical function can be modified using the three β parameters. I_0, I_s, and σ are free parameters that are fit to each star in DoPHOT, while the β parameters are fixed.

The dithered PSF for our images differs slightly from the standard WFPC2 PSF; the stars in our image are generally more symmetric in the combined image than in the single exposures. Therefore, we determined the shape parameters separately for each filter and each of the four WFPC2 chips. The shape parameters were determined as follows: Given a set of parameters, the analytic function was fit to a set of 15 to 20 isolated stars with high signal to noise. The fit was then subtracted from the image and the rms deviation from the sky background was measured. The shape parameters were varied and this process repeated for each set. The set that produced the lowest rms deviation was chosen as the best fit. During this process, we assumed cylindrical symmetry so that $\sigma_x=\sigma_y$ and $\sigma_{xy}=0$. Table 2 lists the PSF parameters used in our photometry.

Because DoPHOT uses an analytic function for its model PSF, there remains a pattern of residuals in the image after a star is subtracted. In addition, DoPHOT assumes a Gaussian PSF when calculating the fit magnitude, which is not quite correct since the PSF differs from a Gaussian shape. The missed flux and non-Gaussian PSF lead to a systematic difference between the fit magnitude and an aperture magnitude measurement. This difference was corrected by comparing the fit magnitudes of the brightest stars with a 0.″5 aperture magnitude. The aperture correction was fit to the difference between these two measurements, and was allowed to vary linearly across the chip to account for a varying PSF. This variation was found to be very small because the dithering technique produced a uniform PSF across each chip. The derived corrections are given in Table 3.

Coordinate transformations between the lists of stars in each filter band were determined using the matching algorithm of Groth (1986) on the brightest 25–30 stars in each list. Each list was transformed to a common coordinate system, and then matched within a specified radius. Stars which

TABLE 3. Aperture correction (mag) $a+b\times10^{-5}x+c\times10^{-5}y$.

Filter	Chip	a	b	c
B	1	−0.42	−17	−37
	2	−0.18	−9	−2
	3	−0.26	−1	2
	4	−0.21	−1	0
V	1	−0.40	−9	3
	2	−0.22	−6	0
	3	−0.28	1	1
	4	−0.22	−1	−5
I	1	−0.42	−11	−5
	2	−0.21	−3	1
	3	−0.26	−3	−2
	4	−0.23	−1	−2

have more than one matching star within this radius are eliminated. We accepted stars identified and measured in *V* and at least either *B* or *I*.

The choice of matching radius is complicated by the presence of "warm pixels" in the WFPC2 chips. Figure 4 shows the distribution of pixel values within a blank piece of sky on one of the WF chips after cosmic-ray rejection. The "warm pixels" are the positive, non-Gaussian tail on the distribution. These "warm pixels" can result from several things, including very faint, unresolved stars and low level cosmic rays. In addition, pixel sensitivity can vary on short time scales. Thus, the "warm pixels" could have been undercorrected by the dark or flat-field image, which might have been taken some time before or after the actual observations. Because the WFPC2 PSF is very narrow, individual "warm pixels" can be misidentified as real stars by DoPHOT. Primarily this affects the matching process between filters. Figure 5 shows the distribution of matched stars with radius and magnitude. At the faint end, there are many matches at large radii. These are false matches with either "warm pixels" or neighboring stars detected in only one filter. Assuming the false matches are distributed uniformly, the number of such matches should increase as the radius squared. Therefore, to eliminate as many false matches as possible, we used a small matching radius.

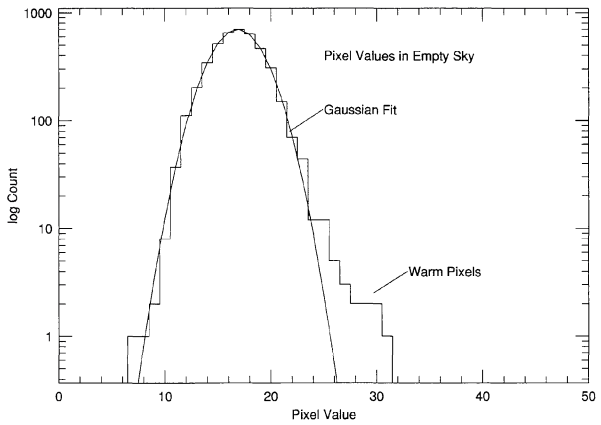

FIG. 4. The distribution of pixel values in an empty sky region is not Gaussian. The histogram shows the number of pixels with a given value within an blank sky region on a WF chip. The overlaid curve is a least squares fit of a Gaussian. On the positive side are clearly non-Gaussian values, corresponding to "warm pixels." The "warm pixels" can result from several effects, including: very faint, unresolved stars; low level cosmic rays; pixels that have been undercorrected by the dark or flat-field image. These "warm pixels" can be mis-identified as stars.

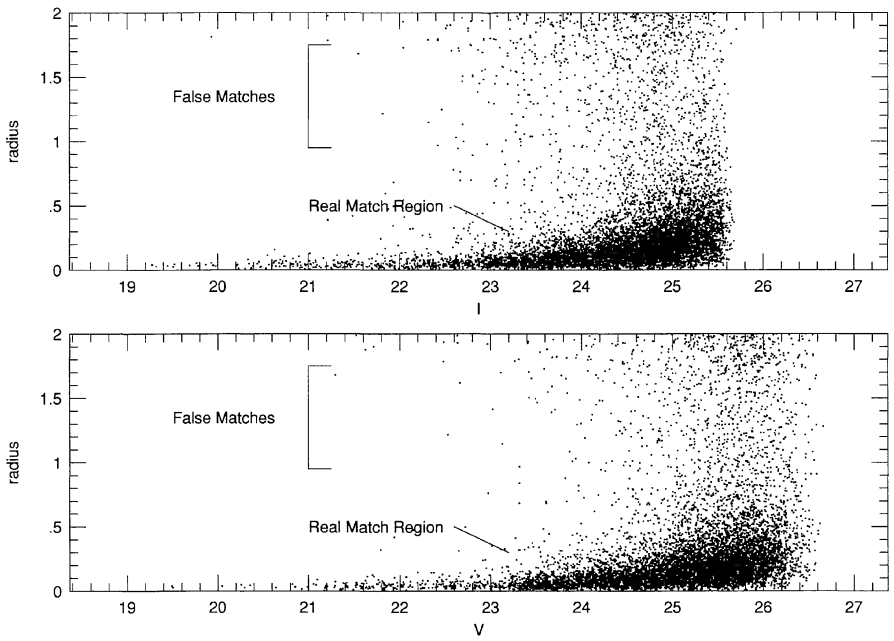

FIG. 5. False matches can occur when matching stars between filters. This is demonstrated in the distribution of separation distance with magnitude for stars matched between *V* and *I* on chip 2. The main concentration of points at small radii is the region of true matches, while the scatter of points at high radii are false matches. The false matches can either be with "warm pixels" or stars detected in only one filter. Excluded from the plot are stars that have more than one match within a 2 pixel radius. We expect the number of false matches to increase with the square of the radius for a uniform density of stars. To eliminate as many false matches as possible, we chose a very small matching radius, 0.7 pixels for the WF chips. Note that the false matches are not clearly separated from the true matches, so there there will be some contamination in our data by false matches.

TABLE 4. Matching data.

Chip	Matching Radius (pixels)	Galaxies			Matched		Multiples	
		B	*V*	*I*	*B&V*	*V&I*	*B&V*	*V&I*
1 (PC)	0.8	2	9	2	511	1149	0	0
2	0.7	15	71	39	4257	6852	11	10
3	0.7	16	50	38	3929	5805	0	6
4	0.7	11	52	25	2773	5096	16	10

TABLE 5. Cross matching data.

	Number matched			% contamination		
	2&3	3&4	2&4	2&3	3&4	2&4
B	62	40	62	0.9	0.6	0.9
V	320	235	247	4	4	4
I	154	133	116	2	2	2

We chose to use the Gaussian width of the PSF, σ, as given in Table 2, for the matching radius. Such a small radius does eliminate some real matches, but this is greatly offset by the number of false matches eliminated, making the faint-end photometry much more reliable. The number of matched stars and multiply matched stars within this radius is given in Table 4.

Also listed in Table 4 are the number of "galaxy" type objects. Such an object is identified by DoPHOT as being broader than the typical stellar image. An attempt is then made to fit the object with two or more stars. If an adequate fit is not achieved, it is assumed to be a galaxy. The images of these identified objects fall into two categories. Either they are broader and more elliptical, and are likely background galaxies, or they occur in crowded regions where several stellar images have blended together. The small fraction of possible blended objects is one indication that crowding is not a problem for the limits achieved by these observations.

To estimate the degree of contamination from false matches, we matched the star lists from two different fields using the same matching radius as was used between filters. The fields do not overlap, so there are no true matches. Figure 6 shows the distribution of matched stars with magnitude. The number of matches increases with fainter magnitudes. There are two reasons for this. One, the number of stars, and, therefore, the density of stars, increases with fainter magnitude. Two, warm pixels will have faint magnitudes. The number of matches found is given in Table 5. The average stellar density in the WF chips is about 1 star per 100 pixels. Thus, we would expect a false matching rate of about 1% in random fields. The actual matching rate we found is about this, or slightly higher. It could be higher because the stellar density is higher than average in some locations, e.g., the young association in the Southeast, boosting the number of false matches. We are encouraged by the low percentage of false matching. It indicates that the number of false matches is no larger than a few percent, and, therefore, not a large source of error in our counting statistics.

2.2 Calibration

We attempted to use the ground-based photometry as the calibration source for the *HST* data. Unfortunately, this was

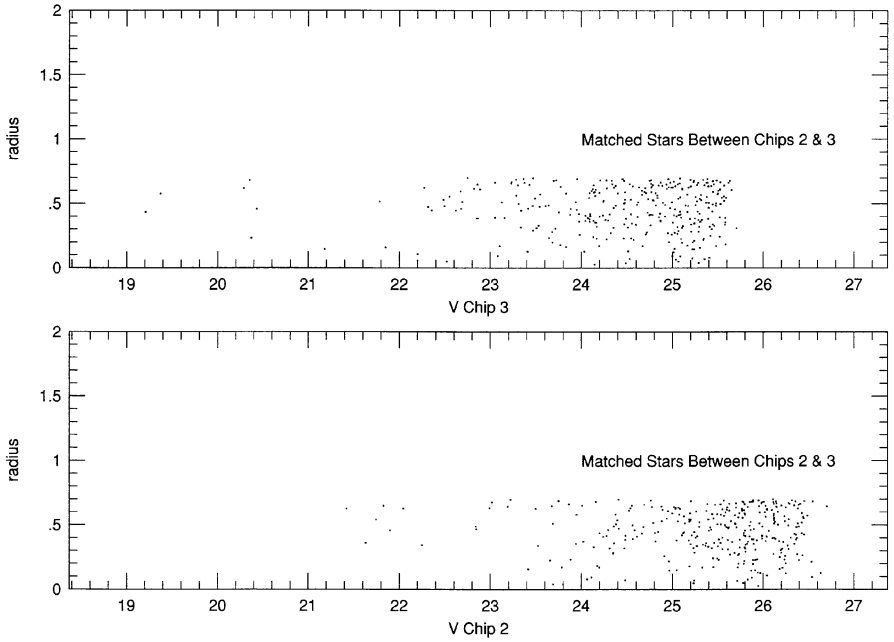

FIG. 6. To measure the degree of contamination by false stars, we matched stars between chips. The chips do not overlap, so there are no true matches. We used the same matching radius as when matching between filters on the same chip. The distribution shows that the false match rate increases with radius, and toward faint magnitudes. The number of matches is a few percent of the input number of stars. This rate is slightly higher than 1%, which is what we would expect based on the average stellar density. The extra few percent of false matches may be due to warm pixels misidentified as stars, and regions in the galaxy with above average stellar density.

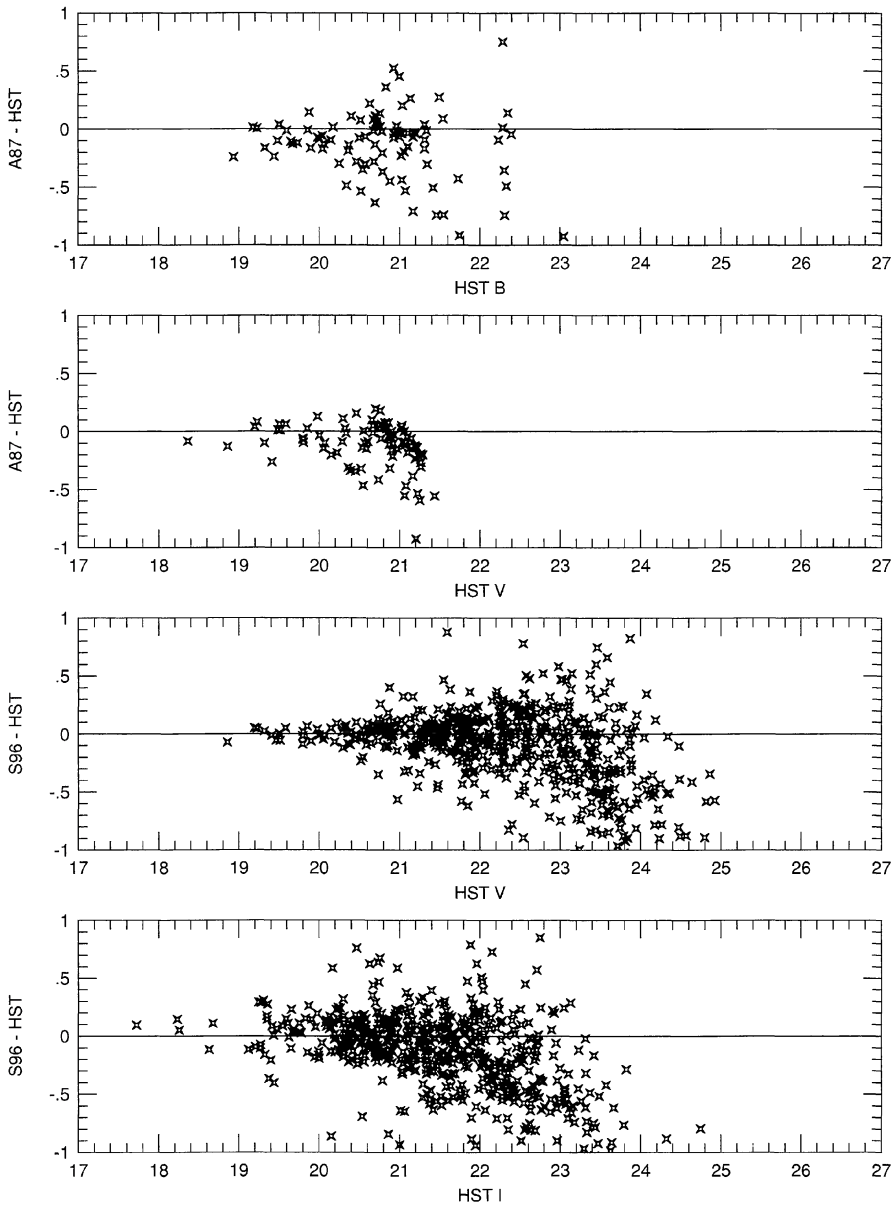

FIG. 7. We compare here previously published ground-based photometry with the *HST* photometry in this paper. The top two plots compare the *B* and *V* photometry with the brightest stars extracted from A87. The bottom two plots compare *V* and *I* photometry generously supplied by S96. The comparisons for *V* brighter than ~21 are very good, giving us confidence in the calibration of Holtzman *et al.* (1995). The zero point offsets for A87 are 0.02 in *B* and 0.005 in *V*. The offsets for S96 are 0.01 in *I* and 0.001 in *V*. The ground-based photometry of fainter stars are affected by crowding confusion. The confused stars have light from more than one star, and, thus, appear brighter than the single stars from the *HST* data with which they are matched.

not very successful. If we used the entire magnitude range available, the ground-based data introduced a bias in the calibration because of crowding problems, which will be discussed below. This bias made the magnitudes appear too bright. If we restricted the magnitude range to the brightest stars, we did not have enough stars to cover all 4 WFPC2 chips, and the calibration varied too greatly from chip to chip.

In the end, we found the calibration given in Holtzman *et al.* (1995) to be more reliable. We compared this calibration with ground-based *V* and *I* photometry generously supplied by Shoko Sakai (from S96). The star lists were matched using the Groth (1986) algorithm to determine the coordinate transformation, as described above. Figure 7 shows the magnitude difference between matched stars. The overall match is extremely good for magnitudes brighter than ~21: 0.001 in *V* and 0.01 in *I*. We also compared the *B* and *V* calibration with the brightest stars extracted from A87. This comparison also looks extremely good. The zero point offset for stars brighter than ~21 is 0.005 in *V* and 0.025 in *B*. The excellent agreement between our calibration and that of S96 and A87 gives us confidence in the accuracy of the standard WFPC2 calibration of Holtzman *et al.* (1995) for these data.

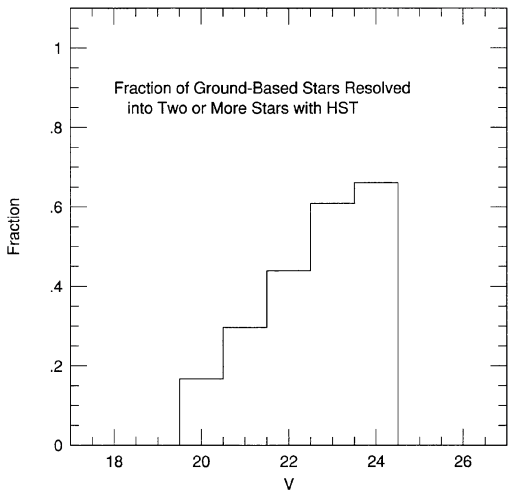

FIG. 8. Shown is the fraction of ground-based stars that are resolved into two or more stars by the *HST*. The ground-based observations come from S96. Included in this fraction are all stars that have more than two *HST* stars closer than 1″. We did not include stars if more than 85% of the light is due to a single star.

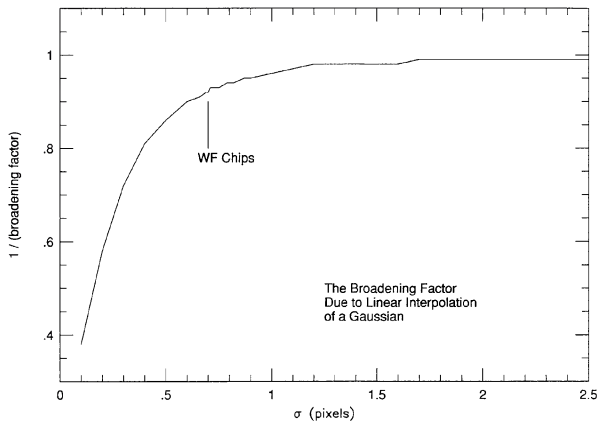

FIG. 9. A function that is undersampled will be artificially broadened when it is linearly interpolated onto another grid. We measured this broadening factor on a Gaussian profile as a function of the standard deviation width. The standard deviation is measured in pixels, so the smaller this value, the larger the degree of undersampling. This broadening factor was used to correct for the linear interpolation used when creating artificial stars.

The comparison of stars fainter than ~21 is not as favorable. There are two noticeable trends in Fig. 7. First, the scatter increases because the photometry errors increase toward fainter magnitudes. Second, the ground-based photometry is systematically too bright. This second trend can be explained by crowding problems from the ground. Many of the stars seen from the ground are actually two or more stellar images blended together. The magnitude of these composite stars will be artificially high because the light from several stars is merged. The superior resolution of the *HST* can resolve these composite stars into their individual stellar components. Thus, the composite stars will be systematically too bright compared to the single *HST* stars with which they are matched.

We have calculated the fraction of stars from S96 that are resolved into two or more stars as a function of magnitude (Fig. 8). Included in this fraction are all S96 stars that have more than two *HST* stars closer than 1″. We did not include stars in this fraction if more than 85% of the light is due to a single star. Ground-based observations of stars fainter then $V\sim22$ are severely hampered by crowding. This is an unfortunate difficulty that limits the accuracy of ground-based photometry of stars in galaxies at distances similar to that of Sextans A.

The final calibration is a correction for reddening. Sextans A is at a fairly high galactic latitude (40°), so this correction is expected to be small. The reddening maps in Burstein & Heiles (1984) give $E(B-V)=0.018$ for the location of Sextans A. The RC3 catalog lists the B-band extinction, including both Galactic and internal, as $A_B=0.13$. They use a conversion of $A_B=4.3E(B-V)$, which gives $E(B-V)=0.03$. We adopt here $E(B-V)=0.03$. Assuming $R_V=3.3$, the conversions of Cardelli *et al.* (1989) give extinction ratios $A_B/A_V=1.326$ and $A_I/A_V=0.485$. Based on this, we used extinction corrections of $A_B=0.13$, $A_V=0.10$, and $A_I=0.05$. These corrections have been applied to the data presented in this paper. As a check on the reddening correction, we have compared theoretical isochrones with the color-color diagram (see Sec. 3).

2.3 Completeness

To measure the completeness of our photometry measurements we performed artificial star tests. In order to place artificial stars at arbitrary positions with respect to the pixel centers, we needed to construct a model PSF for each chip and filter. This was done by averaging together between 15 and 20 isolated stars with high signal to noise. Each star was scaled to unity peak intensity and the centroids were aligned. The scaling was determined by fitting the DoPHOT PSF model to each star [Eq. (1)]. To increase the sampling of the model, it was then placed on a subraster with twice the resolution as the WFPC2 chips through linear interpolation. Through this interpolation, the model is effectively convolved with the sampling pixels. Because the WFPC2 PSF is undersampled, this broadens the stellar image. However, this broadening can be quantified and corrected. Figure 9 shows the degree of broadening of a Gaussian as a function of the standard deviation width. The model PSF can be altered to correct for this broadening by decreasing the radius from the centroid by the broadening factor. To conserve flux, the model values are then increased by the square of the broadening factor. Figure 10 demonstrates a Gaussian profile before and after the broadening correction is applied. For our images the model PSF is broadened by a factor 1.10 ± 0.02.

We performed photometry on 100 frames containing artificial stars for each chip and filter. The frames were created from the real image by adding artificial stars totaling 2% of the real stars detected. The artificial stars were given a uniform distribution in space. The $B-V$ and $V-I$ colors were uniformly chosen at random from the range -1 to 2. The V magnitude was chosen randomly with a power law distribution matching that of the real stars. The overall luminosity function of the real stars is approximately

$$N\propto(m_V)^{0.44}. \quad (3)$$

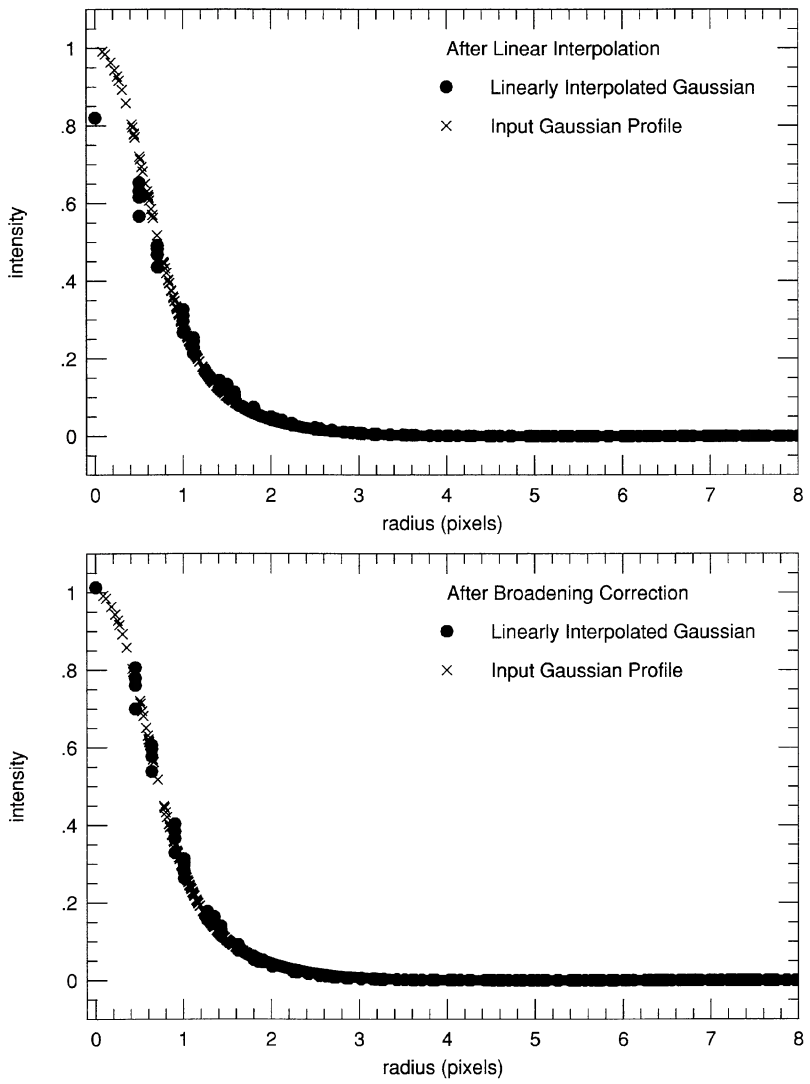

FIG. 10. A function that is linearly interpolated onto an undersampled grid will be artificially broadened. We tested this by interpolating a Gaussian onto an undersampled grid. The top plot shows the input Gaussian plots and the interpolated profile. The broadening effect can be quantified and corrected. A comparison of the corrected interpolation and the input points is shown in the bottom plot. This correction factor was used in constructing artificial stars.

Poisson noise was added to the false star values. The photometry extraction was then performed identically on each frame using DoPHOT. The stars were matched between filters, using the same matching radius as the real frames. Finally, the star lists were matched to the input artificial star lists. This matching radius was chosen to be 0.5, so that only detections within one pixel of the input location are accepted.

Figure 11 shows the fraction of stars recovered. The dashed line represents the completeness as a function of input magnitude. At the faint end, the input magnitude is not the same as the average detected magnitude because of a form of Malmquist bias. There are some stars with input magnitude fainter than the detection limit, which nonetheless have been detected. This is because random noise has scattered these stars above the detection limit. Before we can apply the incompleteness correction to the data we must account for this bias, otherwise the completeness is overestimated in the faintest bins. Figure 11 shows as a solid line the corrected histogram as a function of the detected magnitude.

Note that the completeness is not quite 100% at intermediate magnitudes, e.g., 22 to 24 in V. Stars not recovered in this range are detected by DoPHOT, but do not make it through the matching routines. As discussed above, some real matches are eliminated because we chose a small matching radius. In addition, stars matched with more than one star are eliminated from the list. Thus, real matches can be eliminated for either of these reasons. This can happen either when matching between filters or when matching the artificial star input list with the recovery list. The elimination of these real matches lowers the completeness, even at the bright end, by a few percent.

Furthermore, the cutoff in I is much steeper than in V. I is the primary limitation in the V and I CMD, thus, there are many stars detected in V that are elimated because they were

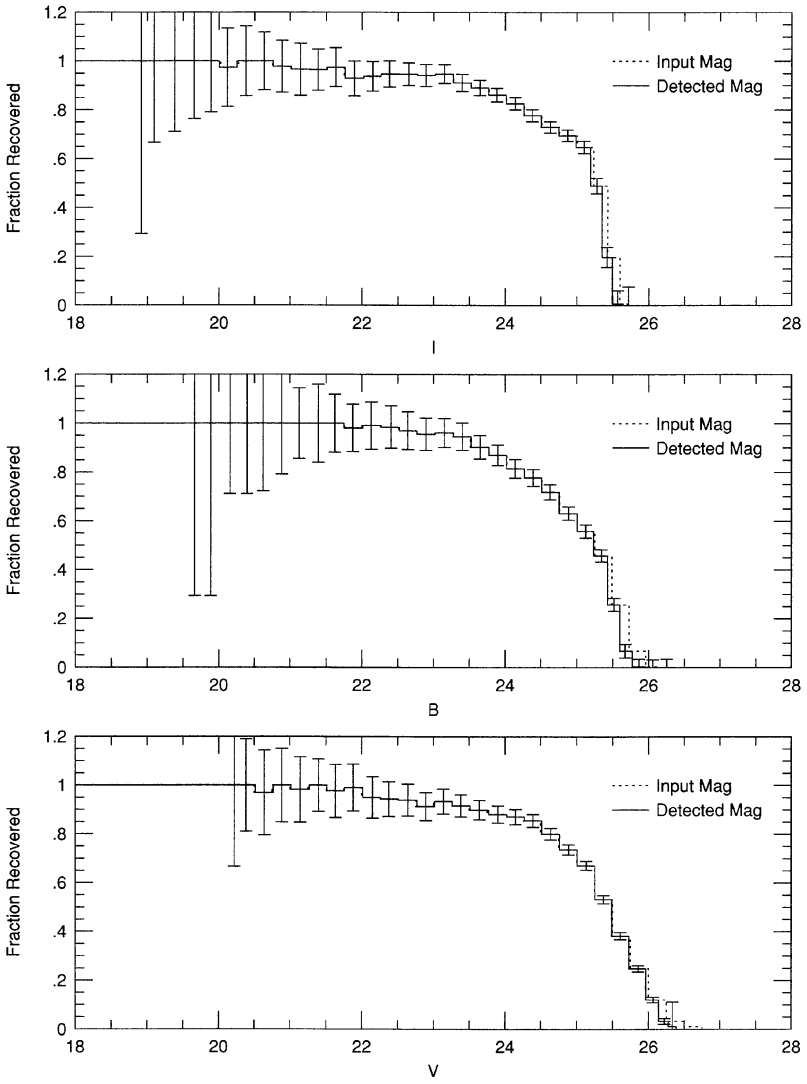

FIG. 11. We performed artificial star tests to determine the completeness of our data. The input artificial stars had a random color and position, with a luminosity function matching that of the real stars. The dashed line is the completeness level as a function of the input magnitude with 0.25 mag bins. Because of Malmquist bias, we detect some stars at an input magnitude fainter than the detection limits; the noise scatters these stars into brighter magnitudes. The solid line is the histogram corrected to be a function of the detected magnitude. The error bars reflect Poisson counting statistics. Our photometry is deepest in *V*, followed by *B* and then *I*. Note, *I* has a much sharper cutoff than *V*. This is because *I* is the primary limitation in the depth of the CMD. Thus, many stars detected in *V* are eliminated in the matching process because they were not detected in I.

not detected in *I*. This flattens the *V* cutoff. There is a similar effect in the *B* and *V* CMD, where *B* is the primary limiting magnitude.

As a check on the random photometric errors reported by DoPHOT, we can compare the input magnitude with the detected magnitude of the artificial stars. Figure 12 shows the absolute difference between input and detected as a function of the input magnitude. Also plotted is a line showing the average difference. The average difference follows the error curve shown in Fig. 2 quite well. We are thus confident that the random photometric errors reported by DoPHOT are an accurate representation of the uncertainties. At the faintest end, the average seems to spike upward to large differences. This is expected in light of the Malmquist bias discussed above, which would bias the faintest detections to a large difference.

3. PHOTOMETRY RESULTS

Figures 13–15 show the CMDs and two-color diagram for this data set. These stars have been corrected for reddening, as discussed in Sec. 2.2. Approximately 11 000 stars were matched in *B* and *V*, while 19 000 stars were matched in *V* and *I*. Of these, 70% have errors better than 0.2 mag.

For the given photometric limits and the distance of Sextans A, the most significant benefit of using the *HST* to do photometry within Sextans A is the lack of crowding problems in the image. As mentioned above, the average density is one star per 100 pixels. This is also apparent by the low number of multiple matches (Table 4). This allows more accurate photometry on bright stars, as well as brightness limits that are ~3 mag fainter than what can be achieved from the ground. These limits were achieved with a rela-

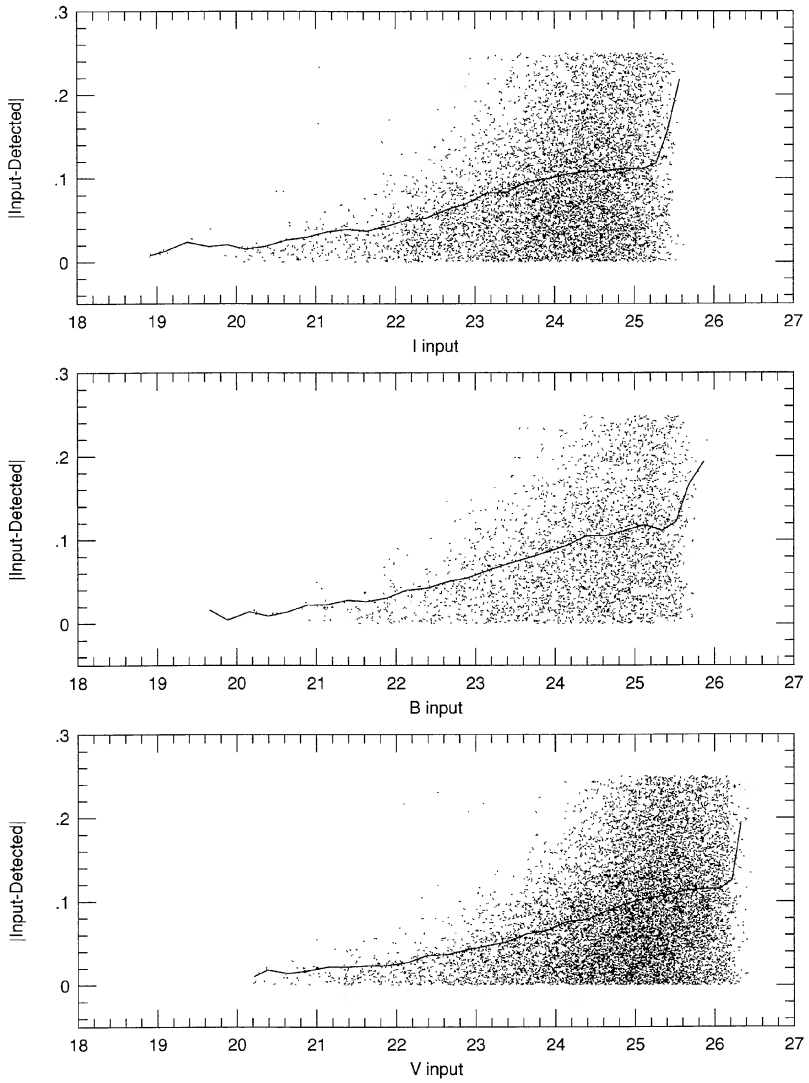

FIG. 12. A comparison of the absolute difference between the artificial star input magnitude and the detected magnitude. The plots have been placed on the same scale as Fig. 2 for ease of comparison. The line shows the average difference as a function of magnitude. This average matches very well the error curve in Fig. 2, indicating the random photometric errors reported by DoPHOT are accurate representations of the uncertainty. The faintest end is biased toward a large difference because of the Malmquist bias discussed in Sec. *2.3*.

tively small number of orbits (1 orbit in each of V and I and 2 in B).

This accuracy has produced a highly detailed CMD with many clearly identifiable populations. There is a dense RGB, as well as a Red Clump just at the limit of photometry. This is strong evidence for an underlying population at least several Gyr old. We can estimate the distance to Sextans A based on the magnitude of the tip of the RGB. We estimate this magnitude to be $I=21.8\pm0.1$ (see Fig. 13). Lee *et al.* (1993) give $M_I=-4$, which implies a distance modulus of 25.8, in excellent agreement with previous measurements. The absolute magnitude scale assuming this distance is plotted on the right of the the CMDs (Figs. 13 & 14).

In addition to the old population, there are very young and intermediate age stars in the CMD. This is readily apparent from Hα imaging and the presence of bright blue stars. From the ground, the blue side of the CMD appears as a single population, which has been called the "blue plume." With the *HST* data, we have been able to photometrically resolve the "blue plume" into two populations. On the blue side is a very young MS. The MS contains very massive stars which are as young or younger than 10 Myr. Just redward of the main sequence is a clearly separate population of bright blue stars. The position of this population in the CMD corresponds with massive stars in their core Helium burning phase (HeB stars). These are stars in the bluest extent of the so-called "blue-loop" phase. From the ground-based observations, these blue HeB stars could not be distinguished from the MS because of limitations in the photometry. The corresponding red HeB stars in the redest extent of the "blue-loop" stars are also seen just above the RGB.

This is the first time that blue HeB stars have been unambiguously identified in a low metallicity system. Several young clusters in the Magellanic Clouds contain stars that

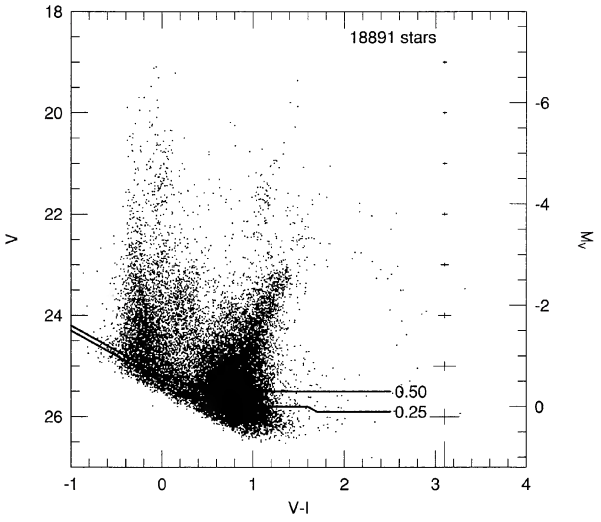

FIG. 13. The CMD in V and I for Sextans A. The photometry has been corrected for interstellar reddening. The crosses on the right indicate the average error at the given V magnitude. The thick lines indicate the completeness at levels 0.25 and 0.50. The right axis shows the absolute V magnitude assuming a distance modulus of 25.8. There are several prominent features. One is the main sequence on the blue side of the diagram. Just redward of the main sequence is a separate population of core Helium burning stars. On the red side, the RGB is well defined, and there are hints of the red clump just at the photometric limits.

are possibly blue HeB stars (e.g., NGC 330, Caloi *et al.* 1993; NGC 2004, Caloi & Cassatella 1995). But, unambiguous identification is difficult because such stars are few in number and come from a single age population. Methods for classifying these stars have so far relied on comparisons with the uncertain stellar evolution models of high mass stars (Subramaniam & Sagar 1995). There is still much debate

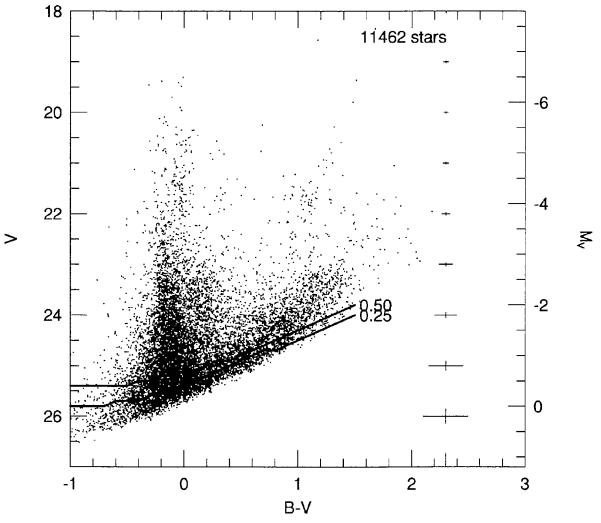

FIG. 14. The CMD in V and B for Sextans A. The photometry has been corrected for interstellar reddening. The crosses on the right indicate the average error at the given V magnitude. The thick lines indicate the completeness at levels 0.25 and 0.50. The right axis shows the absolute V magnitude assuming a distance modulus of 25.8. The main sequence and HeB stars are distinct features on the blue side of the diagram. The B photometric limit is not low enough to define the RGB well.

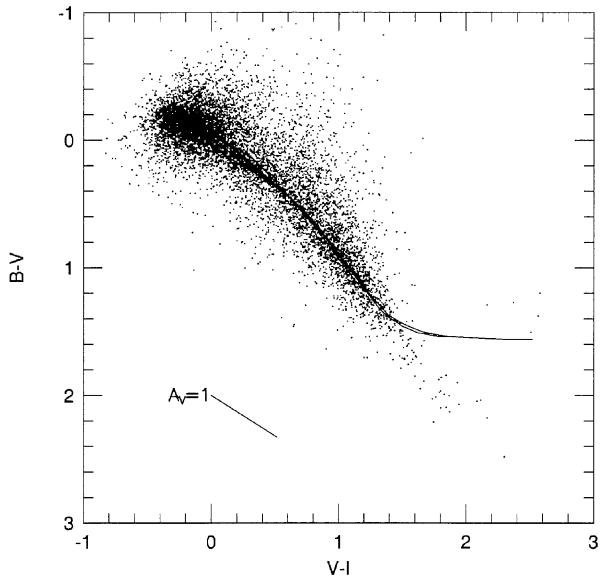

FIG. 15. The two-color diagram for Sextans A. The photometry has been corrected for interstellar reddening. Plotted in the lower left is the reddening line for $A_V=1$. The lines plotted over the data are from theoretical isochrones from Bertelli *et al.* (1994). The isochrones are for a metallicity of $Z=0.001$, and ages of 10 Myr, 100 Myr, and 1 Gyr. The isochrones align very well with the locus of points, giving us confidence in the reddening correction. The isochrones do deviate from the observations for the asymptotic giant branch at $(B-V)$ redder than 1.5.

concerning their correct classification. For example, Grebel *et al.* (1996) argue that these stars are MS blue stragglers. In Sextans A, the identification is clear. Primarily this is because there are stars with a continuous age distribution. Thus, there are over 1000 stars that occupy a well-defined track through the CMD, which can be picked out without reliance on stellar evolution models.

These stars provide an important comparison with theoretical models of massive star evolution beyond the MS. Furthermore, the magnitude of the HeB stars is well correlated with age over the past 1 Gyr (see Bertelli *et al.* 1994). Thus, these stars can be used to determine the star formation history of Sextans A, independent of the MS. These issues will be discussed more thoroughly in Paper II.

As a check on the adopted reddening, we have compared the color-color diagram with theoretical isochrones (Fig. 15). The isochrones were taken from Bertelli *et al.* (1994) for a metalicity of $Z=0.001$. The isochrones line up extremely well with most of the stars. The exception is the asymptotic giant branch stars. The models seem to flatten out at $B-V \sim 1.5$, but the observed stars are redder than this.

Finally, we estimate the contamination by Galactic field stars. Ratnatunga & Bahcall (1985) calculate the Galactic stellar density toward globular clusters based on the Bahcall & Soneira model (1980). The nearest globular cluster to Sextans A from this list is Pal 3, located at $l=240°$, $b=42°$ (6° from Sextans A). The total stellar density down to $V=27$ in this direction is 3.35 stars per square arcminute. The WFPC2 field covers a total of 5.66 square arcminutes, so the total number of expected Galactic stars in our sample is ~ 20. This is extremely small compared to the number of stars

identified in Sextans A. Given this small degree of Galactic field star contamination, we made no attempt to remove or correct for them.

4. CONCLUSIONS

We have extracted photometry of the resolved stars of Sextans A from *HST*, WFPC2 images. The photometry measurements were performed with a version of the PSF fitting program DoPHOT optimized for the undersampled WFPC2 chip. The WFPC2 exposures were dithered which produced more symmetric and uniform stellar profiles. This aided DoPHOT in identifying faint stars. We also found that, unlike aperture photometry, the PSF fitting routine was not affected by intra-pixel sensitivity variation of the WFPC2 chips.

The photometry was calibrated with the standard Holtzman *et al.* (1995) equations. This proved to be accurate to ~ 0.01 mag in comparison to previously published ground-based data. Using artificial star tests we have determined that the photometry set is 50% complete down to $V=25.6$, $B=25.4$, and $I=25.3$.

The WFPC2 images are not hampered by crowding for the given photometric limits and the distance of Sextans A. This allows very accurate and deep CMDs compared to ground-based photometry. There are several clearly defined populations in the CMDs.

- A MS younger than 10 Myr.
- Blue HeB stars, in the bluest extent of the "blue-loop" phase of evolution. These stars are in the age range of 10 to 1000 Myr.
- A prominent RGB indicating an underlying older population (>1 Gyr).

This is the first time the blue HeB stars have been clearly identified in a low metallicity system such as Sextans A. From the ground, these stars have blended with the MS to form what has been called the blue plume. These stars provide an important comparison with theoretical models of massive star evolution at low metallicity. These stars also provide a means to determine the star formation history of the galaxy independent of the MS.

In Paper II we compare the young stellar populations in the CMD with theoretical models of stellar evolution. Based on this comparison, we construct the star formation history for Sextans A over the past 600 Myr. Paper III will analyze the older stellar population, and try to extend the star formation history further back in time.

Use of the *HST* provides the opportunity to resolve stars in Local Group dwarf galaxies, such as Sextans A, to very faint limits. This allows us to construct detailed star formation histories for a wide variety of galaxies with different environments, metallicities, and gas content. Such histories will provide important clues to the star formation process that we can apply to larger galaxies. An understanding of how stars form will eventually allow us to determine how galaxies form, and how they evolve.

We are grateful to Shoko Sakai for providing us V and I ground-based photometry for comparison with our data. We thank the referee for many useful comments which have helped improve this paper. We would also like to thank Bob Benjamin, Don Garnett, Chip Kobulnicky, Barron Koralesky, and Tess Lavezzi for many fruitful discussions. This work was partially supported by NASA Grants No. STScI/GO-5915, No. NAGW-3189, and No. NAG5-3373.

REFERENCES

Aparicio, A., Garcia-Pelayo, J. M., Moles, M., & Melnick, J. 1987, A&AS, 71, 297 (A87)
Aparicio, A., & Rodriguez-Ulloa, J. A. 1992, A&A, 260, 77
Bahcall, J. N., & Soneira, R. M. 1980, ApJS, 44, 73
Bertelli, G., Bressan, A., Chiosi, C., Fagotto, F., & Nasi, E. 1994, A&AS, 106, 275
Bertelli, G., Mateo, M., Chiosi, C., & Bressan, A. 1992, ApJ, 388, 400
Burrows, C. J. (Ed.) 1994, Wide Field and Planetary Camera 2 Instrument Handbook (STScI, Baltimore)
Burstein, D., & Heiles, C. 1984, ApJS, 54, 33
Caloi, V., & Cassatella, A. 1995, A&A, 295, 63
Caloi, V. Cassatella, A., Castellani, V., & Walker, A. 1993, A&A, 271, 109
Cardelli, J. A., Clayton, G. C., & Mathis, J. S. 1989, ApJS, 345, 245
de Vaucoulers, G., de Vaucoulers, A., Corwin, Jr., H. G., Buta, R. J., Paturel, G., & Fouqué, P. 1991, Third Reference Catalog of Bright Galaxies (Springer, New York)
Dohm-Palmer, R. C., *et al.* 1997, AJ, 114, 2527 (Paper II)
Gallagher, J. S., & Hunter, D. A. 1984, ARA&A, 22, 37
Gallagher, J. S., *et al.* 1996, ApJ, 466, 732
Gallart, C., Aparicio, A., & Vilchez, J. M. 1996a, AJ, 112, 1928
Gallart, C., Aparicio, A., Bertelli, G., & Chiosi, C. 1996b, AJ, 112, 1950
Gallart, C., Aparicio, A., Bertelli, G., & Chiosi, C. 1996c, AJ, 112, 2596
Grebel, E. K., Roberts, W. J., & Brandner, W. 1996, A&A, 311, 470
Groth, E. J. 1986, AJ, 91, 1244
Hodge, P., Kennicutt, R. C., & Strobel, N. 1994, PASP, 106, 765
Hoessel, J. G, Schommer, R. A., & Danielson, G. E. 1983, ApJ, 274, 577
Holtzman, J. A., Burrows, C. J., Casertano, S., Hester, J., Trauger, J. T., Watson, A. M., & Worthey, G. 1995, PASP, 107, 1065
Hunter, D. A., & Plummer, J. D. 1996, ApJ, 462, 732
Lee, M. G., Freedman, W. L., & Madore, B. F. 1993, ApJ, 417, 553
Marconi, G., Tosi, M., Greggio, L., & Focardi, P. 1995, AJ, 109, 173
Mateo, M. 1988, ApJ, 331, 261
Piotto, G., Capaccioli, M., & Pellegrini, C. 1994, A&A, 287, 371
Ratnatunga, K. U., & Bahcall, J. N. 1985, ApJS, 59, 63
Richer, M. G., & McCall, M. L. 1995, ApJ, 445, 642
Saha, A., Sandage, A., Labhardt, L., Tammann, G. A., Macchetto, F. D., & Panagia, N. 1996, ApJ, 466, 55
Sakai, S., Madore, B. F., & Freedman, W. L. 1996, ApJ, 461, 713 (S96)
Sandage, A., & Carlson, G. 1982, ApJ, 258, 439
Schechter, P. L., Mateo, M. L., & Saha, A. 1993, PASP, 105, 1342
Skillman, E. D. 1996, The Minnesota Lectures on Extragalactic Neutral Hydrogen, ASP Conf. Ser. 106 (ASP, San Francisco), p. 208
Skillman, E. D., Kennicutt, R. C., & Hodge, P. W. 1989, ApJ, 347, 875
Skillman, E. D., Terlevich, R., Teuben, P. J., & van Woerden, H. 1988, A&A, 198, 33
Smecker-Hane, T. A., Stetson, P. B., Hesser, J. E., & Lehnert, M. D. 1994, AJ, 108, 507
Subramaniam, A., & Sagar, R. 1995, A&A, 297, 695
Tolstoy, E. 1996, ApJ, 462, 684
Tolstoy, E., & Saha, A. 1996, ApJ, 462, 672
Tosi, M., Greggio, L., Marconi, G., & Focardi, P. 1991, AJ, 102, 951
Walker, A. R. 1987, MNRAS, 224, 935

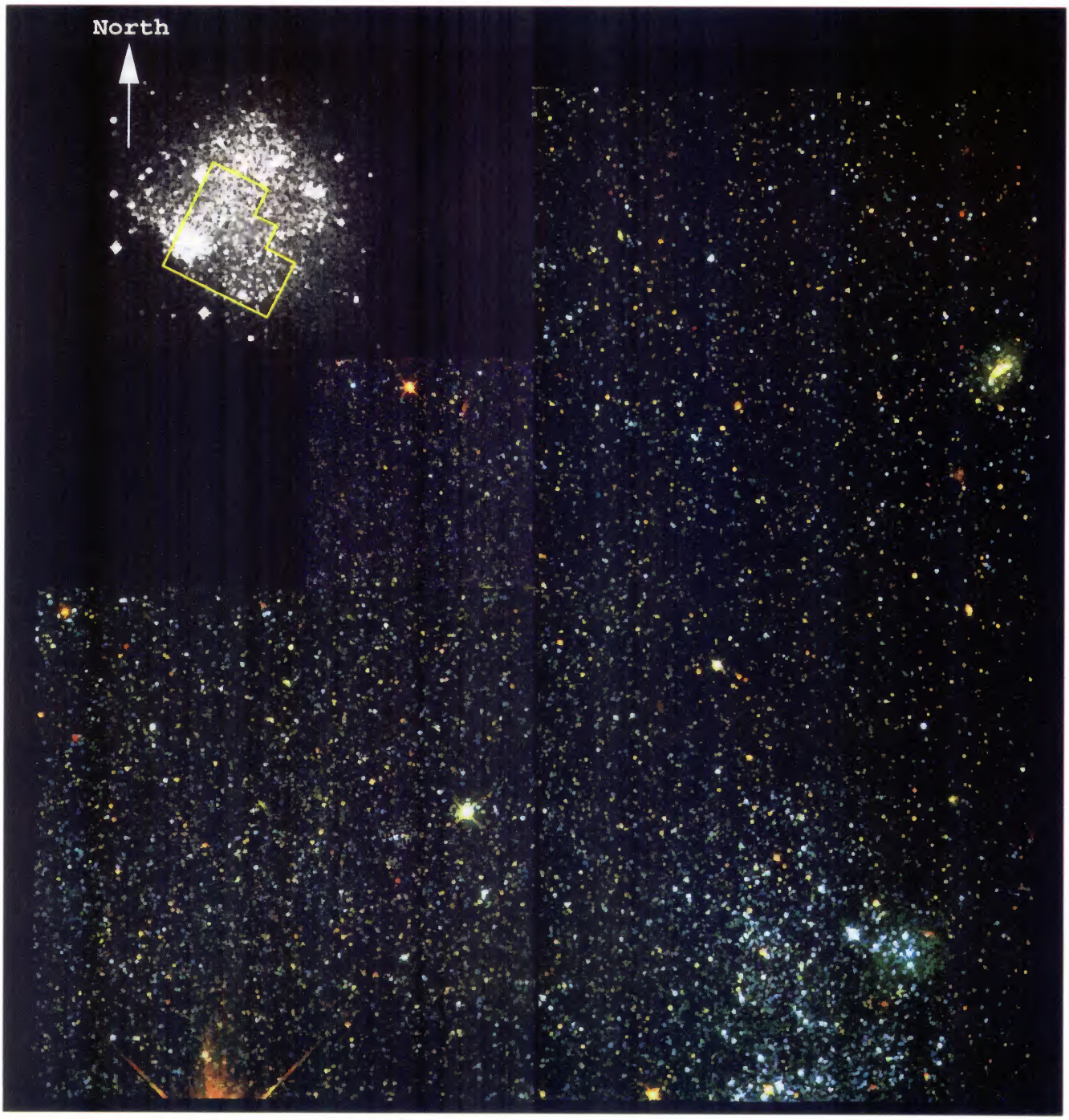

FIG. 1. A true color reproduction of the *HST* WFPC2 image of the dI galaxy Sextans A. The inset in the upper left is the Digitized Sky Survey image with the WFPC footprint overlaid. For this inset North is up and East is to the left. The most prominent feature in this view of the galaxy is an association of young blue stars in the lower right corner (Southeast).

Dohm-Palmer *et al.* (see page 2515)